

UCLA

UCLA Previously Published Works

Title

Evaluation of the impact of strain correction on the orientation of cardiac diffusion tensors with in vivo and ex vivo porcine hearts

Permalink

<https://escholarship.org/uc/item/8gx3h8rx>

Journal

Magnetic Resonance in Medicine, 79(4)

ISSN

0740-3194

Authors

Ferreira, Pedro F
Nielles-Vallespin, Sonia
Scott, Andrew D
[et al.](#)

Publication Date







2018-04-01

DOI

10.1002/mrm.26850

Peer reviewed

Evaluation of the Impact of Strain Correction on the Orientation of Cardiac Diffusion Tensors With In Vivo and Ex Vivo Porcine Hearts

Pedro F. Ferreira ^{1,2,*} Sonia Nielles-Vallespin,³ Andrew D. Scott ^{1,2} Ranil de Silva,^{1,2} Philip J. Kilner,^{1,2} Daniel B. Ennis,⁴ Daniel A. Auger,⁵ Jonathan D. Suever,⁶ Xiaodong Zhong ⁷ Bruce S. Spottiswoode ⁸ Dudley J. Pennell ^{1,2} Andrew E. Arai,³ and David N. Firmin ^{1,2}

Purpose: To evaluate the importance of strain-correcting stimulated echo acquisition mode echo-planar imaging cardiac diffusion tensor imaging.

Methods: Healthy pigs ($n = 11$) were successfully scanned with a 3D cine displacement-encoded imaging with stimulated echoes and a monopolar-stimulated echo-planar imaging diffusion tensor imaging sequence at 3T during diastasis, peak systole, and strain sweet spots in a midventricular short-axis slice. The same diffusion tensor imaging sequence was repeated ex vivo after arresting the hearts in either a relaxed (KCl-induced) or contracted (BaCl₂-induced) state. The displacement-encoded imaging with stimulated echoes data were used to strain-correct the in vivo cardiac diffusion tensor imaging in diastole and systole. The orientation of the primary (helix angles) and secondary (E2A) diffusion eigenvectors was compared with and without strain correction and to the strain-free ex vivo data.

Results: Strain correction reduces systolic E2A significantly when compared without strain correction and ex vivo (median absolute E2A = 34.3° versus E2A = 57.1° ($P = 0.01$), E2A = 60.5° ($P = 0.006$), respectively). The systolic distribution of E2A without strain correction is closer to the contracted ex vivo distribution than with strain correction, root mean square deviation of 0.027 versus 0.038.

Conclusions: The current strain-correction model amplifies the contribution of microscopic strain to diffusion resulting in an overcorrection of E2A. Results show that a new model that considers cellular rearrangement is required. **Magn Reson**

Med 000:000–000, 2017. © 2017 International Society for Magnetic Resonance in Medicine.

Key words: cardiac; diffusion tensor imaging; strain; microstructure; cardiomyocyte; sheetlets

INTRODUCTION

Myocardial micro-architecture is remarkably complex. Cardiomyocytes exhibit a transmural helical organization with helix angles (HAs) rotating smoothly from positive in the endocardium to negative in the epicardium (1–3). Additionally, cardiomyocytes have a laminar organization, in which sheets of cardiomyocytes are surrounded by collagen-lined shear layers, as found histologically in many explanted mammalian hearts (4–7). These myolaminae play a major role in the radial thickening and longitudinal shortening during the heart cycle (8–12). The collective rotation of sheetlets accommodated by shear layer slippage, driven by cardiomyocyte contraction, is the dominant contributor to the radial thickening and longitudinal shortening observed in vivo. Much smaller contributions arise from sarcomere-driven changes in cardiomyocyte shape (13). Because myolaminae are discrete and exist only very locally, Hales et al. referred to them as “sheetlets” (14).

Cardiac diffusion tensor imaging (cDTI) is an MR imaging technique that encodes the self-diffusion of water molecules in three dimensions. A diffusion tensor is calculated for each voxel, and several diffusion related parameters can be extracted. The orientation of the tensor is closely linked to the voxels’ microstructure. It has been shown that the principal direction of diffusion aligns with the cardiomyocyte long axis, whereas the secondary and tertiary directions of diffusion provide cross-cardiomyocyte sheetlet-plane and sheetlet-normal directions, respectively (15–20). More recent ex vivo cDTI studies have been performed with hearts in relaxed and contracted states, thus probing microstructural reorganization during contraction (14,21). No substantial changes of HA were measured, but the sheetlet planes were found to rotate from almost perpendicular to the local myocardial wall in systole to more wall parallel in diastole, in agreement with current models of sheetlet rotation during cardiac contraction.

¹Cardiovascular BRU, Royal Brompton Hospital, London, United Kingdom.

²National Heart and Lung Institute, Imperial College, London, United Kingdom.

³NHLBI, National Institutes of Health, Bethesda, Maryland, USA.

⁴Department of Radiological Sciences, University of California, Los Angeles, California, USA.

⁵Biomedical Engineering, University of Virginia, Charlottesville, Virginia, USA.

⁶Geisinger Medical Center, Danville, Pennsylvania, USA.

⁷Siemens Healthcare, Atlanta, Georgia, USA.

⁸Siemens Healthcare, Knoxville, Tennessee, USA.

*Correspondence to: Pedro Ferreira, Ph.D., Cardiovascular BRU, Royal Brompton Hospital, London, SW3 6NP, United Kingdom. E-mail: p.ferreira@rbht.nhs.uk

This work was supported by the British Heart Foundation; the National Institute of Health Research Cardiovascular Biomedical Research Unit at the Royal Brompton Hospital and Imperial College, London; and the National Heart, Lung, and Blood Institute, National Institutes of Health, Division of Intramural Research, Department of Health and Human Services (HL004607-14CPB). D. P. receives research support from Siemens, and is a stockholder and director of Cardiovascular Imaging Solutions. D. F. receives research support from Siemens.

Received 20 March 2017; revised 7 June 2017; accepted 2 July 2017

DOI 10.1002/mrm.26850

Published online 00 Month 2017 in Wiley Online Library (wileyonlinelibrary.com).

In vivo cDTI has attracted renewed interest aided by new technical advancements in both hardware and pulse sequence design (22–26). Dou et al. in 2002 reported in vivo rotation of sheetlets toward a more radial conformation during systolic contraction in one healthy volunteer (27). More recent studies confirm a similar pattern of sheetlet rotation in a cohort of healthy volunteers and abnormal sheetlet dynamics in cardiomyopathy patients (28–30).

Two common approaches exist for encoding diffusion in vivo: a motion-compensated spin echo with the encoding lasting for only a few tens of milliseconds (24,26), and a monopolar stimulated (STEAM) approach in which diffusion is encoded over an entire cardiac cycle (31). The spin-echo approach encodes diffusion in a single heartbeat, although the diffusion-encoding time is approximately two orders of magnitude shorter when compared with the STEAM approach, which results in probing smaller microstructural length scales and concomitantly higher measured diffusivities (32–34).

A STEAM approach takes full advantage of cardiac motion being periodic, with the diffusion encoding/decoding gradients applied when the heart is at the same position in successive cardiac cycles. This technique requires breath-holding or dedicated respiratory triggering. However, a well-known disadvantage of the STEAM approach is regularly debated: cardiac strain sensitivity. Even though the heart returns to its original position, measuring diffusion with a STEAM sequence requires consideration of the myocardium’s strain history during the diffusion-encoding period (35–37). Recently we have successfully acquired in vivo cDTI data on both healthy and cardiomyopathy patients with a monopolar STEAM echo-planar imaging (EPI) sequence with both intra- and intercenter reproducibility (28,30,38,39), but questions about strain effects remained unanswered, in particular the effects on the measurement of sheetlet rotation between systole and diastole.

Myocardial strain throughout the cardiac cycle can be measured and subsequently apply a correction to the diffusion tensor data acquired in systole or diastole (29,36). However, the current strain-correction model ignores sheetlet rotation as a major contributor to wall thickening, and therefore likely to “correct” the diffusion data for an exaggerated strain effect.

The objective of this study was to evaluate the effect of strain-correcting cDTI data by directly comparing in vivo cDTI data with and without strain correction according to the established model proposed by Reese et al. (36), with strain-free ex-vivo DTI data of the same porcine hearts arrested in a diastolic-like or systolic-like conformations.

METHODS

The porcine cDTI data analyzed in this study are part of a larger data set that was used previously to compare in vivo, in situ, and ex vivo DTI scans with histology, in which no strain analysis or correction was applied (30). Here, we report data from a subset in which the 3D strain was acquired successfully. A shortened version of this work was presented at the Society for Cardiovascular Magnetic Resonance 2017 (40).

Experimental Design

Animal procedures were approved by the National Heart, Lung, and Blood Institute Animal Care and Use Committee. Sixteen Yorkshire pigs (weight 30 to 35 kg) were studied. Anesthesia was induced with the use of atropine, butorphanol, ketamine, and xylazine and maintained with the use of inhaled sevoflurane and supplemental IV propofol, together with mechanical ventilation.

All imaging was performed at 3 T (MAGNETOM Skyra, Siemens, Erlangen, Germany) using investigational prototype sequences, a phased-array Siemens torso coil, and spine array combination. The mean cardiac cycle length was 737 ± 82 ms.

Following initial scans, which included breath-hold retro-gated cines, the pigs were scanned with a multislice cine displacement-encoded imaging with stimulated echoes (DENSE) sequence with 3D displacement encoding (41) covering the entire left ventricle (LV), to obtain 3D strain tensors throughout the entire cardiac cycle. This was followed by cDTI acquisitions in one midventricular slice at multiple time points throughout the cardiac cycle, including diastasis and peak systole, as determined from a short-axis cine in the same plane.

All animals were subsequently euthanized under anesthesia in either a “diastolic-like” state with an intravenous administration of KCl (4 meq/kg) ($n = 8$), or a “systolic-like” state by intravenous administration of BaCl₂ (40 meq/kg) ($n = 8$). The hearts were excised and rinsed in normal saline. Preparation followed the protocols described by Kung et al. (18). The coronary arteries were flushed, and the cardiac chambers filled with vinyl polysiloxane (Microsonic Inc, Ambridge, PA). The hearts were placed in a cylindrical container filled with a susceptibility-matching fluid (Fomblin Y-LVAC 6-06, Solvay Solexis, Neward, DE) and were supported using open-cell foam. The cDTI was then repeated in the static excised hearts for a midventricular slice using the same sequence as used in vivo. This slice was visually positioned to match the in vivo slice as much as possible.

Strain Imaging

A free-breathing, navigator-gated, 2D multislice spiral cine DENSE imaging with 3D displacement encoding was performed with contiguous slices covering the entire LV. Sequence parameters included in-plane field of view of 320×320 mm with a voxel size of 2.5×2.5 mm², slice thickness of 8 mm, flip angle of 10°, repetition time of 14 ms, echo time of 1.16 ms, temporal resolution of 32 ms, displacement encoding frequency at 0.10 cycles/mm, and six spiral interleaves.

Although DENSE data were acquired to cover the entire LV, only five slices were used for 3D strain calculation: two slices both above and below the chosen midventricular slice of interest, the remaining slices were discarded. The DENSE data postprocessing matrix was therefore $128 \times 128 \times 5$ pixels.

The 3D strain and right stretch tensors were calculated from the DENSE data for the midventricular slice throughout the cardiac cycle with MATLAB software (The MathWorks, Natick, MA) developed at the University of Virginia (41,42). The initial myocardial segmentation was

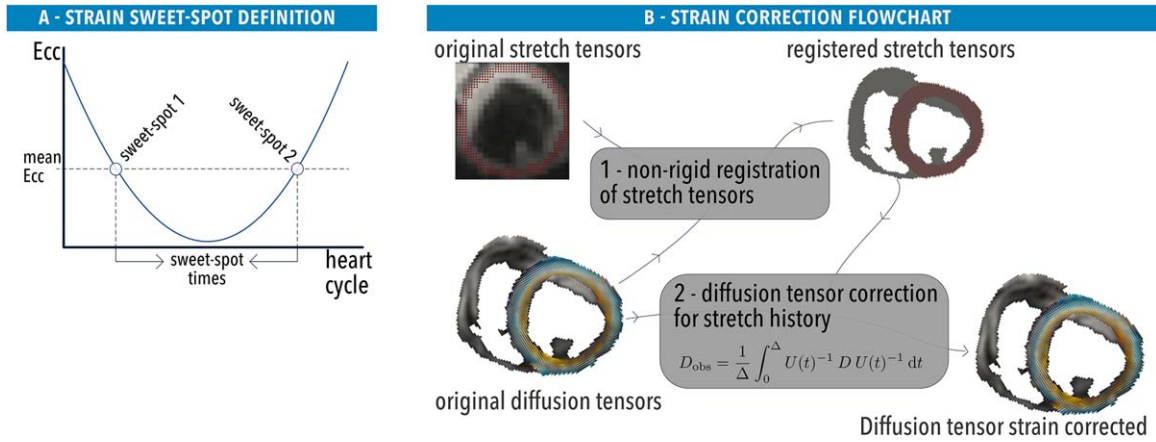


FIG. 1. **a:** Diagram showing how the sweet-spot times are calculated. The sweet-spot times are defined when the measured strain equals its mean value. The mean LV circumferential strain-time curve was used, as the higher number of pixels along the circumferential direction are likely to make it more robust than the radial or longitudinal strain curves. **b:** Flowchart showing how the strain correction cycle is applied to the diffusion tensors. D_{obs} , diffusion tensor before strain correction; $U(t)$, stretch tensor throughout an entire cardiac cycle Δ ; D , diffusion tensor after strain correction.

performed semi-automatically using the open-source software DENSEanalysis (43,44).

The strain data were used for two purposes: first, to identify the two sweet-spot times in the cardiac cycle (Fig. 1a); and second, to derive and register stretch tensors to the diffusion data to be corrected (Fig. 1b) (see Supporting Information).

The components of strain along the local coordinates of the diffusion eigensystem were calculated at peak systole. Torsion was also calculated between the most basal and the most apical slice according to Equation [2] from Rüssel et al. (45).

Diffusion Tensor Imaging

Breath-hold in vivo DTI data were acquired in one midventricular slice at six to nine time points in the cardiac cycle. A STEAM-EPI sequence with a monopolar diffusion-encoding scheme was used with the following b-values: $b_{ref} = 50 \text{ s/mm}^2$ (20 averages) in a single direction; $b = 500 \text{ s/mm}^2$ (20 averages) in six diffusion-encoding directions; and $b = 150 \text{ s/mm}^2$ and $b = 350 \text{ s/mm}^2$ in six directions (two averages). Other parameters included zonal excitation; fat saturation; diffusion weighting time of 1 RR interval; echo time = 30 ms; bandwidth = 1838 Hz/pixel; SENSE parallel imaging acceleration factor of 2; field of view = $320 \text{ mm} \times 120 \text{ mm}$; matrix = 160×60 pixels; EPI echo train length = 30 readouts; echo spacing = 0.65 ms; EPI readout duration = 19.5 ms; spatial resolution = $2 \times 2 \times 8 \text{ mm}^3$ interpolated to $1 \times 1 \times 8 \text{ mm}^3$ by zero-filling k-space. Ex vivo DTI scans were performed with an identical protocol, with a repetition time set to 1400 ms (diffusion time 700 ms).

DTI data were analyzed from only four cardiac phases: diastasis, peak systole, and the two acquisitions closest to the sweet-spot times given by the circumferential strain curve.

The DTI data were postprocessed with software developed in house (MATLAB). The myocardium was manually segmented excluding the right ventricle, blood pool, and

papillary muscle. Three parameters related to the diffusion tensor orientation were extracted: two angles concerning the primary eigenvector: helix angle (HA) and transverse angle (TA); and an angle related to the secondary eigenvector E2A (18,28) (Fig. 2). In contrast to HA, TA and E2A demonstrate no obvious transmural organization; therefore, for simplicity, the median absolute angle is represented without the polarity of the angle. However, for completeness, the angle polarity is included in the DTI parameter maps and histograms. The mean diffusivity (MD) of the diffusion tensor was also calculated.

The diastolic and systolic diffusion tensor data were calculated with and without strain correction, and compared with the sweet spots and to the ex vivo diffusion data of the same midventricular slice.

Wilcoxon rank sum and Kruskal-Wallis (with follow-up pairwise comparisons) tests were used to assess the differences. A P value equal or lower than 0.01 was used for the follow-up pairwise comparisons to reduce the probability of type I errors when performing multiple comparisons. In an initial analysis, we failed to find any consistent significant differences among different sectors of the wall for DTI measures; therefore, we kept our analysis global to reduce measurement noise.

RESULTS

Diffusion tensor data were successfully acquired for all pigs, and 3D strain data were successfully extracted from the DENSE data for 11 of the original 16 pigs. The remaining five pigs had poor-quality DENSE image data and/or phase-unwrapping issues. All subsequent analyses are therefore shown for 11 pigs only (six with a diastolic arrest, five with a systolic arrest). The DTI acquisition trigger time closest to the calculated sweet-spot times was different by $24 \pm 12 \text{ ms}$. Two DTI sweet-spot data sets (of 22) were excluded, as the closest DTI trigger time differed by more than 40 ms. The mean heart rate was 83 bpm (10 bpm), and the LV ejection fraction was 0.49% (0.06%).

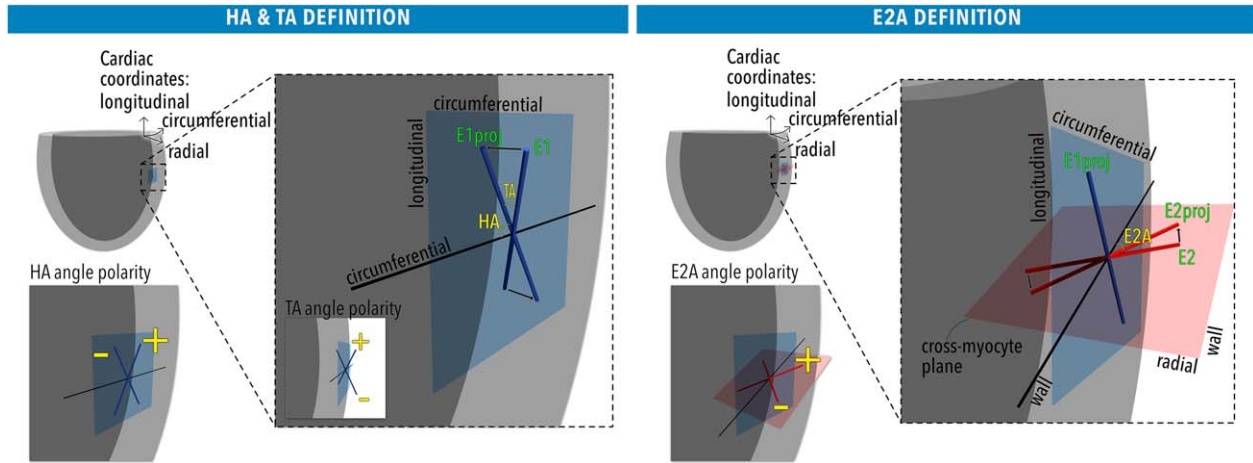


FIG. 2. Diagram showing the definitions of HA, TA, and E2A. To calculate HA, E1 is projected in the local longitudinal-circumferential plane shown in blue (E1proj). The angle between E1 and E1proj defines the TA. The angle of E1proj to the circumferential axis defines the HA. The HA is positive for a right-handed helix when viewed from the apex. The TA is positive if it rotates clockwise from the longitudinal-circumferential plane, and negative if it rotates counterclockwise, when looking along the circumferential axis direction. The projection of E1 is then used to define the plane perpendicular to it, known as the cross-cardiomyocyte plane shown in red. This plane contains two orthogonal directions: the radial direction and the wall tangent direction. The secondary eigenvector E2 is projected into this plane, and the angle between E2proj and the wall-tangent direction defines E2A. E2A is positive if pointing toward the apex, and negative if pointing toward the base.

Strain Measurements

The midventricular mean radial, circumferential, and longitudinal strain-time curves are shown in Figure 3a. The measured mean (standard deviation) peak radial, circumferential, and longitudinal strains were $Err = 0.21$ (0.06), $Ecc = -0.14$ (0.02), $Ell = -0.11$ (0.01). The sweet spots given by the Ecc curves are located at 24% (7%) and 74% (12%) of the RR interval time. Global torsion was 5.3° (1.5°) (Fig. 3b). The largest components of strain are aligned with the sheetlets (Ess positive strain) and with the myocytes

(Emm negative strain). The shear components (Ems, Emn, and Esn) are smaller at peak systole (Fig. 3c).

Diffusion Tensor Data

The measured DTI parameters are given in Table 1. There are significant differences between diastolic and systolic E2A values for in vivo without and with strain correction ($P < 0.001$ and $P = 0.005$, respectively) and for ex vivo ($P = 0.004$). Additionally, there are significant differences for the in vivo transverse angle without strain correction

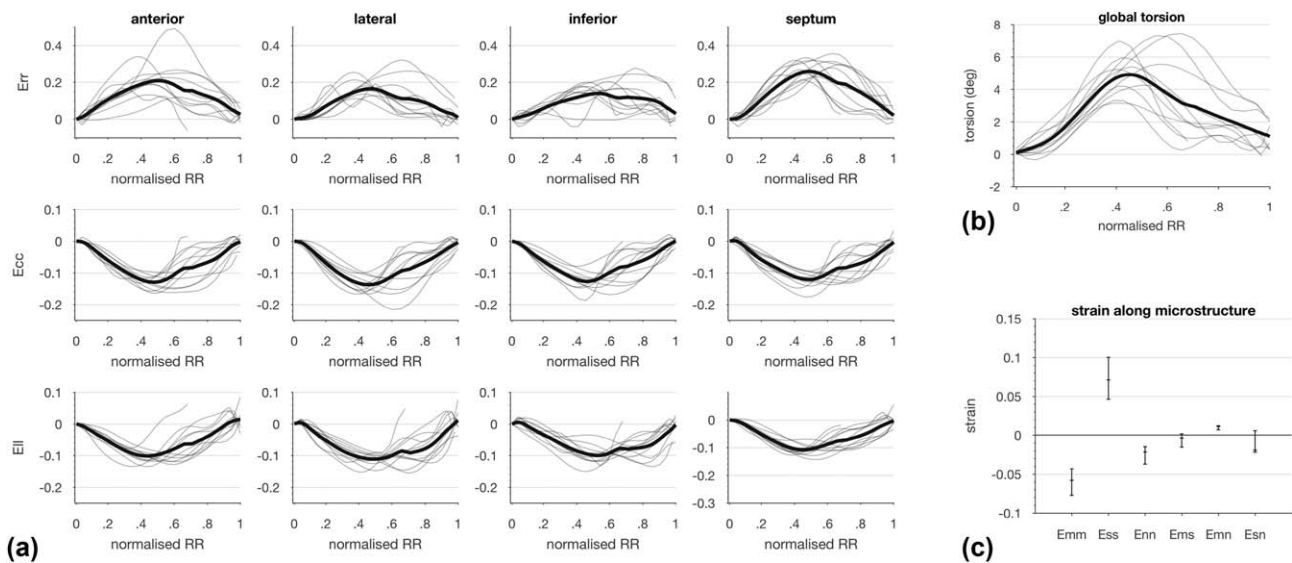


FIG. 3. **a:** Radial (Err), circumferential (Ecc), and longitudinal (Ell) strain curves normalized to the RR interval for the anterior, lateral, inferior, and septum sectors. The thin lines represent the subjects' mean strain curves averaged over the LV slice of interest, and the thick lines represent the intersubject mean strain curve. **b:** Global torsion curves. **c:** Strain tensor components along the diffusion tensor coordinate system at peak systole (mm, along myocytes; ss, along sheetlets; nn, along sheetlet-normal). Shear components: ms, myocyte sheetlet; mn, myocyte sheetlet-normal; sn, sheetlet sheetlet-normal.

Table 1
Diffusion Parameters.

	Without SC		With SC		Sweet spots			Ex vivo arrests	
	Diastole	Systole	Diastole	Systole	Sweet spot 1	Sweet spot 2	Diastole	Systole	
HA range (°)	36.9 (6.9); -52.4 (9.3) (<i>P</i> = 0.14; <i>P</i> = 0.58)	40.3 (4.7); -53.3 (11.8)	35.7 (6.7); -55.7 (16.0) (<i>P</i> = 0.79; <i>P</i> = 0.39)	37.2 (3.9); -47.5 (15.1)	37.8 (4.0); -60.6 (9.0) (<i>P</i> = 0.34; <i>P</i> = 0.92)	31.4 (10.9); -53.7 (13.3)	35.0* (5.0); -51.8* (2.1) (<i>P</i> = 0.004; <i>P</i> = 0.03)	46.5 (3.7); -60.1 (5.2)	
Absolute E2A (°)	12.2* (2.6) (<i>P</i> < 0.001)	57.1 (14.2)	19.3* (8.64) (<i>P</i> = 0.005)	34.3 (11.4)	22.9 (19.2) (<i>P</i> = 0.91)	24.7 (10.0)	18.2* (5.42) (<i>P</i> = 0.004)	60.5 (5.05)	
Absolute TA (°)	6.08* (1.46) (<i>P</i> = 0.015)	7.45 (2.94)	8.3 (2.38) (<i>P</i> = 0.89)	8.67 (1.85)	6.42 (2.17) (<i>P</i> = 0.18)	7.25 (1.29)	5.92 (0.56) (<i>P</i> = 0.13)	7.62 (2.34)	
MD (10 ⁻³ mm ² s ⁻¹)	1.11* (0.07) (<i>P</i> = 0.010)	0.99 (0.12)	1.00* (0.08) (<i>P</i> = 0.001)	1.14 (0.07)	1.05 (0.12) (<i>P</i> = 0.31)	1.10 (0.19)	0.61 (0.09) (<i>P</i> = 0.66)	0.66 (0.11)	

Note: Diffusion parameters in vivo with and without strain correction, at the in vivo sweet spots and at the ex vivo arrested hearts. SC, strain correction; HA range, mean angle range from endocardium to epicardium; TA and E2A, median of the absolute values of all LV myocardial voxels; MD, mean over all LV myocardial voxels. All values are shown as intersubject median (interquartile range). * (red) denotes the statistically significant difference when compared with the corresponding systolic or sweet spot 2 value (*P* < 0.05).

Between-Groups Comparison (Kruskal-Wallis With Follow-up Pairwise Comparisons)

	Without SC versus with SC		Without SC versus ex vivo		With SC versus ex vivo	
	<i>P</i> = 0.98; <i>P</i> = 0.003 <i>P</i> = 0.007 <i>P</i> = 0.26; <i>P</i> = 0.01 <i>P</i> = 0.91	<i>P</i> = 0.72 <i>P</i> = 0.003 <i>P</i> = 0.007 <i>P</i> = 0.72 <i>P</i> = 0.01 <i>P</i> = 0.91	<i>P</i> = 0.59; <i>P</i> = 0.037 <i>P</i> = 0.99 <i>P</i> = 0.047; <i>P</i> = 0.74 <i>P</i> = 0.76	<i>P</i> = 0.48; <i>P</i> = 0.94 <i>P</i> = 0.044 <i>P</i> < 0.001; <i>P</i> = 0.006 <i>P</i> = 0.56		
Diastole	HA range (°)	<i>P</i> = 0.98; <i>P</i> = 0.72	<i>P</i> = 0.59; <i>P</i> = 0.99	<i>P</i> = 0.48; <i>P</i> = 0.77		
	Absolute E2A (°)	<i>P</i> = 0.003	<i>P</i> = 0.037	<i>P</i> = 0.94		
	Absolute TA (°)	<i>P</i> = 0.007	<i>P</i> = 0.99	<i>P</i> = 0.044		
Systole	HA range (°)	<i>P</i> = 0.26; <i>P</i> = 0.72	<i>P</i> = 0.047; <i>P</i> = 0.57	<i>P</i> < 0.001; <i>P</i> = 0.23		
	Absolute E2A (°)	<i>P</i> = 0.01	<i>P</i> = 0.74	<i>P</i> = 0.006		
	Absolute TA (°)	<i>P</i> = 0.91	<i>P</i> = 0.76	<i>P</i> = 0.56		

Note: *P* values when compared between in vivo without and with strain correction and ex vivo arrested. SC, strain correction; HA range, mean angle range from endocardium to epicardium. *(red) denotes the statistical difference (*P* ≤ 0.01; *P*-value threshold with a Bonferroni correction for three multiple tests, conservatively rounded down to 0.01).

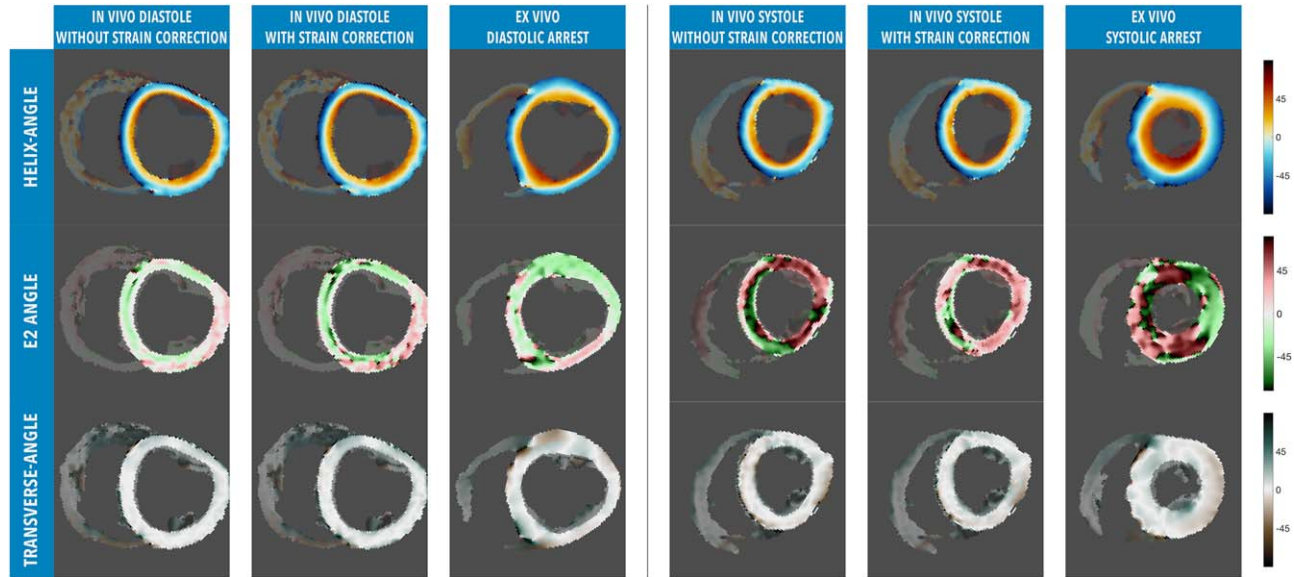


FIG. 4. Example DTI maps of tensor orientation measurements: HA, E2A, and TA for two hearts, one arrested in diastole (left) and one arrested in systole (right).

($P=0.015$), and for the ex vivo HA range ($P=0.004$ to 0.03). No significant differences were found for any measure between sweet-spot 1 and sweet-spot 2. Mean diffusivity was found to be statistically different between diastole and systole for both with and without strain correction ($P=0.01$ and $P=0.001$, respectively), but not for ex vivo ($P=0.66$). The MD is approximately 40% lower for the ex vivo hearts compared with the in vivo.

In addition to measuring changes from diastole to systole, we also compared the in vivo results with and without strain correction with the ex vivo arrested hearts in the same corresponding state (bottom of Table 1). Example maps showing the three DTI orientation measurements in vivo (both with and without strain correction) and ex vivo are shown in Figure 4 for two hearts: one arrested in a relaxed diastolic-like and one in a contracted systolic-like conformation. Visually, HA and TA maps show a similar configuration between diastole and systole, and between without/with strain correction and ex vivo. The E2A maps show pronounced differences between diastole and systole for the data without strain-correction, with strain correction, and ex vivo. The E2A maps in diastole show

low positive and negative angles, whereas in systole they have high positive and negative angles. In both diastole and systole there is a significant difference in E2A between with and without strain correction ($P=0.003$ and 0.01 , respectively). Ex vivo E2As differ significantly from the respective systolic strain-corrected E2A ($P=0.006$), but less so from the diastolic non-strain-corrected E2A ($P=0.037$). Additional angular differences were found between the strain-corrected data and the ex vivo data for the systolic endocardial HA mean values ($P<0.001$) and between the diastolic TA with and without strain correction ($P=0.007$).

The absolute median E2A values from Table 1 are also displayed in a scatter plot (Fig. 5). The mobility of the individual myocardial median E2A values between diastole and systole for the in vivo data without/with strain correction, between the two sweet-spot times, and the respective arrested ex vivo values, are shown. A large rotation of E2 is seen in the non-strain-corrected data from a more wall-parallel conformation in diastole (low angles), to a more wall-perpendicular conformation in systole (high angles). A similar effect is seen in the

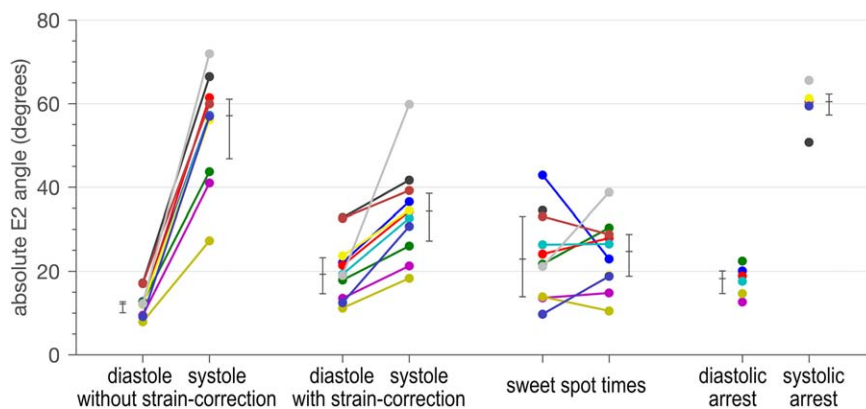


FIG. 5. Median absolute E2A values. The in vivo values show the mobility of E2A from a diastolic to a systolic phase with and without strain correction, and at the two time points closest to the sweet-spot times. The respective color-coded ex vivo hearts are also shown for either a diastolic or systolic arrest.

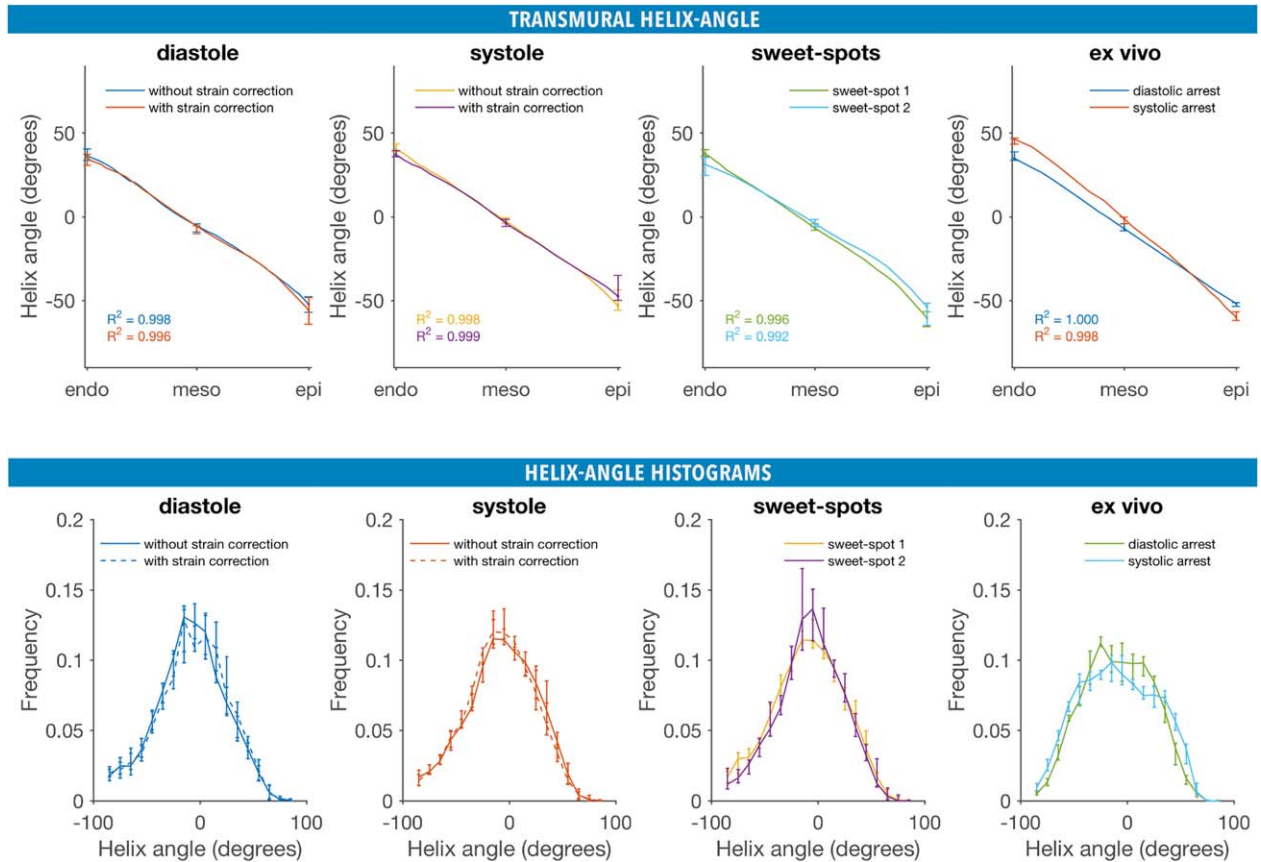


FIG. 6. (top) Mean transmural HA line profiles with intersubject interquartile range at the endocardium, mesocardium, and epicardium. Line profiles are shown for diastole and systole with and without strain correction, at the two sweet-spot times, and for the arrested ex vivo hearts. The R^2 values are the adjusted R^2 for a linear fit. (bottom) The HA histograms of all myocardial voxels at diastole (with and without strain correction), systole (with and without strain correction), the two sweet spots, and for the explanted hearts arrested in a diastolic/systolic-like state. The histogram curves show the intersubject median and interquartile range; bin size is 10° .

strain-corrected data, although the rotation is smaller. The biggest difference between in vivo data with and without strain correction is in the systolic phase, in which the strain-corrected E2A is significantly lower than the non-strain-corrected and the ex vivo contracted systolic-like arrests (median absolute E2A = 34.3° versus E2A = 57.1° ($P = 0.01$), E2A = 60.5° ($P = 0.006$), respectively). As indicated in Table 1, E2A is similar between the two sweet spots.

Figures 6 and 7 provide additional analysis of HA, TA, and E2A. Figure 6 plots the mean transmural HA line profiles, as well as histograms of the myocardial distribution of HA values. There is a linear transmural progression of HA values in all cases, and a slightly wider distribution of HA values in the ex vivo data. No clear transmural organization was found for TA and E2A. Figure 7 shows the distribution of TA and E2A values. There is no apparent difference between the TA with and without strain correction in any of the plots, in contrast to the large differences in E2A. As observed in Figure 5, the systolic distributions of E2A angles without strain correction appear more similar to the ex vivo relaxed and contracted distributions than after strain correction. The in vivo systolic distribution appears to be the most different between with and without strain correction, whereas at the distribution peaks at $\pm 90^\circ$ without strain correction, the peak occurs at a much

lower absolute angle of 25° with strain correction. The combined systolic and diastolic root mean square deviation of the in vivo histograms without and with strain correction to the ex vivo histograms is 0.027 and 0.038, respectively. The in vivo histograms without strain correction are therefore closer to the ex vivo.

DISCUSSION

In previous work we showed that in healthy human hearts there is a significant rotation of E2A as the heart contracts from diastole to systole, whereas the HA remains relatively unchanged; however, the confounding contribution of strain to these results was unclear (28). Subsequent pre-clinical studies have demonstrated a similar pattern of E2A rotation in a porcine model imaged in vivo, and in situ and ex vivo in the absence of strain effects. The similarity of the in vivo, in situ, and ex vivo results enabled us to infer that that potential strain effects must be small, although no strain correction was performed in our previous reports. In this work, we assessed the performance of the standard strain-correction model (35) by directly comparing in vivo DTI data before and after strain correction with ex vivo strain-free data. We believe this to be the first study comparing in vivo diffusion data with and without strain correction with the same hearts after arrest. A

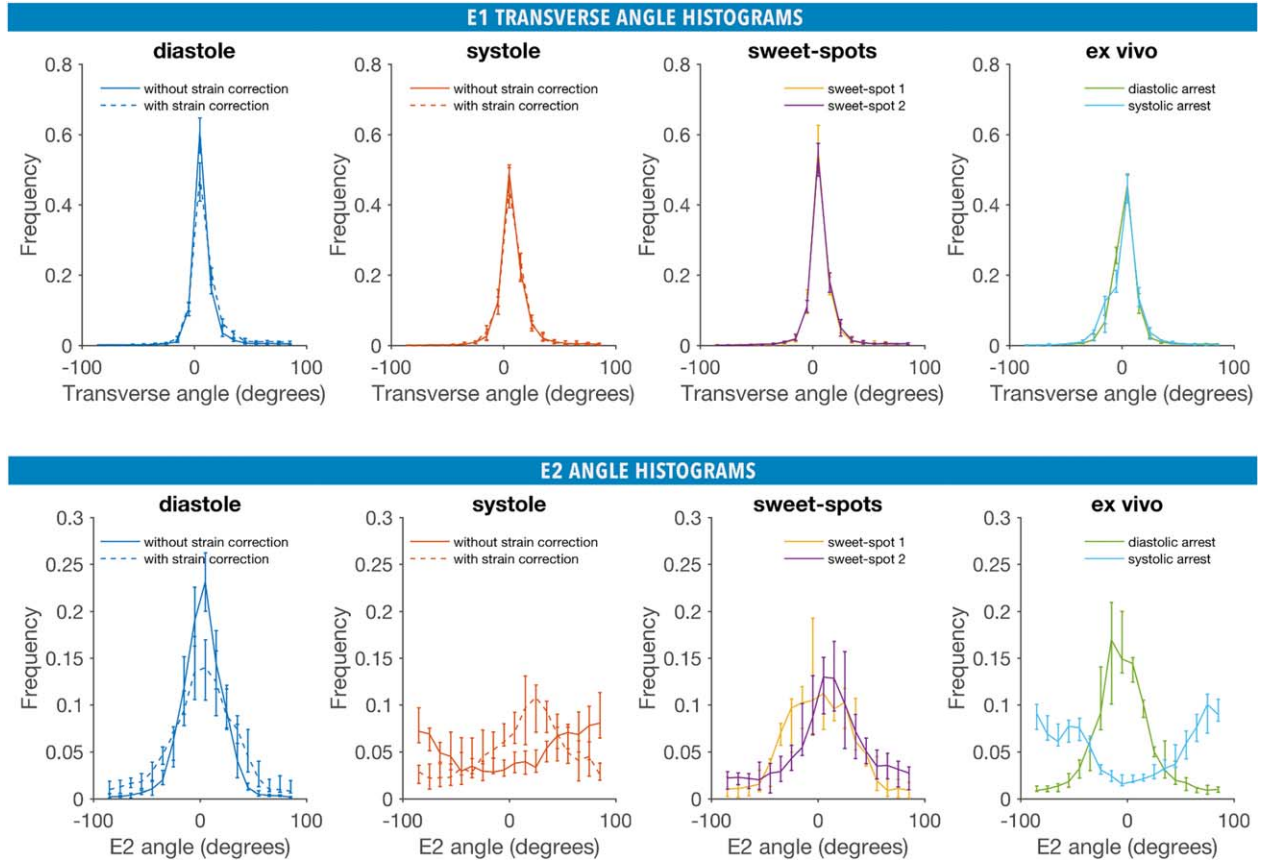


FIG. 7. The TA (top) and E2A (bottom) histograms of all myocardial voxels at diastole (with and without strain correction), systole (with and without strain correction), the two sweet spots, and for the explanted hearts arrested in a diastolic/systolic-like state. The histogram curves show the intersubject median and interquartile range; bin size is 10° .

previous study presented strain-corrected STEAM-EPI data acquired in peak systole and diastole, demonstrating the effects of strain correction (29). However, these studies lacked a ground truth that we have included in the form of ex vivo DTI in the same hearts. Therefore, we were able to quantify the effect of strain on in vivo cDTI and assess the performance of conventional strain correction.

Several important results were found regarding tensor orientation. Changes in HA and TA throughout the cardiac cycle were small, and these parameters were largely unaffected by strain correction. Ex vivo HA and TA values and distribution were similar to in vivo, although the ex vivo HA distribution was flatter than the in vivo counterparts. It is noteworthy that our data showed very low transverse angles at all cardiac phases interrogated, indicating a highly coherent myocyte orientation. In contrast, E2A varies as the heart contracts. Figures 5 and 7 (lower panel) show that in vivo E2A changed from predominantly low absolute angles in diastole to predominantly high absolute angles in systole without strain correction. The same data with strain correction showed a much smaller shift between systole and diastole, with the largest differences observed in systole when pre- and post-strain-correction data were compared. As expected, the distribution of E2A values at the two sweet spots was similar, because the heart was in a similar configuration. When comparing without and with strain-correction

data with the corresponding ex vivo results, in which no tissue strain history is present, the without-strain-correction data more closely resembles the ex vivo distributions of E2A. These results are consistent with a substantial rotation of E2 between diastole and systole, in keeping with current models of cardiac contraction as a result of rotation of sheetlets with shear layer slippage. The current strain-correction model artifactually reduces the measured E2A mobility. As the heart spends a longer proportion of the cardiac cycle in a relaxed rather than contracted state, the effect of strain correction is most marked on data acquired at peak systole.

The change in distribution of E2A angles from diastole to systole was much more pronounced than that measured in a Langendorff perfused rat heart model from Hales et al. (14). More work is needed to ascertain whether this disparity is the result of protocol differences, particularly the shorter diffusion mixing time of the spin-echo sequence used by Hales et al., or anatomical and physiological differences between the two species.

The in vivo results presented here are consistent with those of Stoeck et al. in human hearts (29) and with numerical simulations (Supporting Fig. S1 and Supporting Table S1). Strain correcting the diffusion data significantly reduced E2A mobility, and brought systolic E2A values close to the sweet-spot values where strain effects are minimal. The observation that E2A mobility is reduced by strain correction

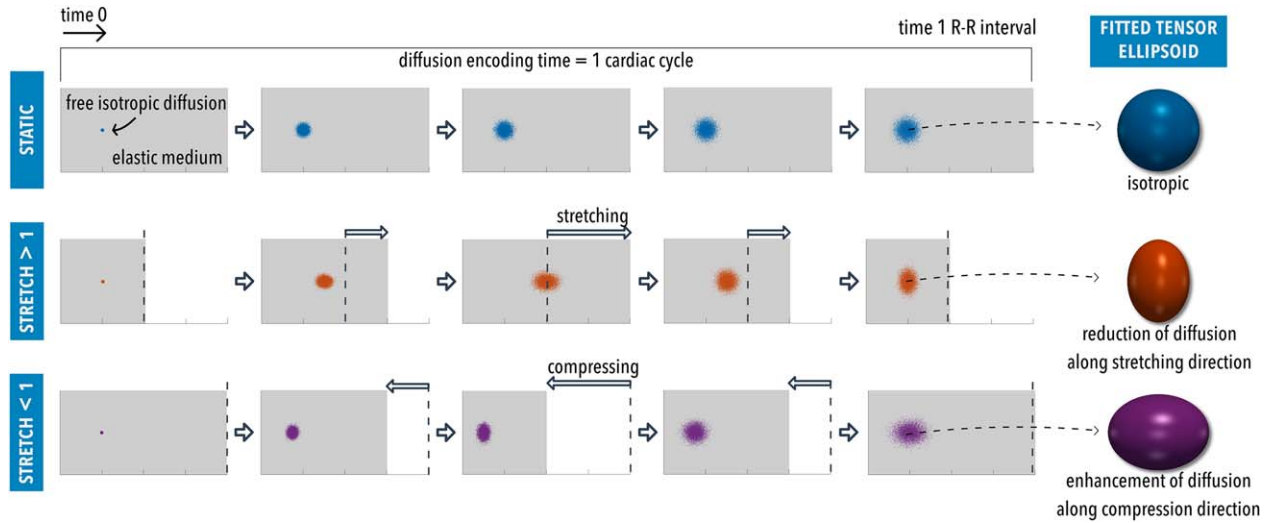


FIG. 8. Simulation of the effects of an elastic stretch on a free diffusion cloud of particles. A stretch > 1 loop of the material during diffusion encoding will result in a reduction of the diffusivity along that direction. A stretch < 1 loop will have the opposite effect.

is not unexpected. Macroscopic tissue strain measured with MRI is intimately connected to cellular rearrangement and sheetlet shear, and therefore directly correlated with E2A mobility as measured by cDTI. As these measures are inextricably interconnected, correcting for macroscopic strain inevitably leads to altered E2A mobility.

The effects of strain correction can be categorized according to three cardiac orthogonal coordinates. The diffusion tensor orientation measures are only affected by strain that has components along the same directions as the respective eigenvectors. For example, the primary eigenvector of diffusion, which defines HA, is commonly aligned close to the longitudinal circumferential plane, with only small components in the radial direction. The HA is therefore minimally affected by radial strain, commonly the direction with the greatest measured strain. Additionally, it was found that the effects of longitudinal and circumferential strain, which are typically of similar amplitude, have opposing effects on HA (Supporting Table S2). This work therefore suggests that the global effect of strain and strain correction on HA is small. In contrast, E2 is primarily affected by the cumulative effect of radial and longitudinal strains, resulting in E2 being affected more by strain correction.

The strain-correction model established by Reese et al. (35) assumes the heart to be formed of a gelatin-like material that is stretched and compressed at different stages of the cardiac cycle. If we are measuring diffusion at peak systole, then while the diffusion is being encoded, myocardial tissue initially shortens radially before contracting to its original position. The diffusion encoding in the radial direction is therefore enhanced by the history of material strain (Fig. 8). Conversely, if measuring diffusion in a diastolic state, then the material will be stretched in the radial direction before coming back to its original position, resulting in a reduction of the measured diffusion in the radial direction. Analogous strain effects will happen in the longitudinal and circumferential direction. This is the basis of the previously proposed strain-correction model:

From the 3D stretch tensor history throughout the cardiac cycle, one can correct the measured 3D diffusion tensor to cancel these strain effects. However, this model assumes a uniform diffusivity throughout the cardiac cycle, with no barriers on the scales we measure diffusion on. Additionally, it assumes that macroscopic cardiac deformation is a result of elastic material stretch only. It is now generally recognized that most of the wall thickening and longitudinal shortening is not caused by cardiomyocyte stretch, but caused by cellular reorganization and transmural shear moderated by its laminar organization. For this reason, it is thought that the previously proposed model may significantly overestimate the effects of microscopic cardiomyocyte strain based on the measured macroscopic tissue deformation.

The work by Sonnenblick et al. measured a reduction of 15% in the length of the cardiomyocyte sarcomere in the canine heart (13), which results in approximately 8% increase in radius for incompressible cardiomyocytes. The in vivo median wall thickening in this study was approximately 28%. Assuming we have similar cardiomyocyte sarcomere length and radius changes in the porcine heart, then approximately 30% of the macroscopic wall thickening could be the result of microscopic cardiomyocyte strain. Microstructural strain and reorganization of the tissue will therefore affect the measured tensor, but the model required to describe this is highly complex and yet to be elucidated. In this paper, we primarily analyze tensor orientation, but there is an important rotational invariant measure that we should discuss: MD. Mean diffusivity provides a measure of the mean square distance diffused by water molecules in a given time. With the STEAM sequence, diffusion is encoded over an entire heart cycle. Diffusivity measurements will depend on myocyte shape, strain, and perfusion effects; all three vary throughout the cardiac cycle. Without strain correction, MD decreases between diastole and systole (1.11 to $0.99 \times 10^{-3} \text{ mm}^2\text{s}^{-1}$; $P=0.01$), and the opposite happens with strain correction (1.00 to $1.14 \times 10^{-3} \text{ mm}^2\text{s}^{-1}$; $P=0.001$). A similar result

was found by Stoeck et al. in the human heart (29). The measured ex vivo diffusivities are approximately 40% lower, which is expected when diffusion measurements change from body temperature to room temperature. Importantly, there is no significant change in MD ex vivo from diastole to systole ($P=0.66$), in which no strain or perfusion effects are present.

We have simplified the TA and E2A analysis by calculating the median value from the absolute distribution, ignoring angle polarity. We believe this to be a valid simplification because the signed TA and E2A distributions from Figure 7 appear symmetric. The median value of absolute E2A is therefore a measure of sheetlet tilt relative to the local heart wall.

In this work, we assume that the ex vivo arrested relaxed and contracted conformations approximate to diastole and systole in vivo. Because of the lack of blood-pressure loading, the arrested contracted heart wall thickness was found to be 140% of the in vivo systolic wall thickness. Histology of these ex vivo pig hearts after fixation was performed for another study, and sheetlet and shear layer orientations were found to correlate to diffusion E2 orientation measured with DTI in both ex vivo and in vivo data (30). Therefore, we believe that the ex vivo contracted systolic-like state approximates the in vivo conformation of the microstructure.

There are two important limitations to this work: the low number of animals studied, and the available spatial resolution of current in vivo MR measurements of strain and diffusion. Diffusion tensor estimation from a voxel containing a large number of cardiomyocytes and myolaminae can only be meaningful if there is coherence of the microstructure. Histology studies have observed two populations of counter-sloping sheetlets and shear layers (18); more advanced diffusion techniques will be required to interrogate these multiple populations (46). The accuracy of radial and longitudinal strain is also affected by the low spatial resolution used in DENSE imaging. Porcine strain values measured in this work were found to be lower than typical values measured in humans; therefore, the effects of strain correction are expected to be greater in humans. The DENSE cine imaging uses prospective echocardiogram gating; therefore, the latest stages of the cardiac cycle may not be imaged. Some of the individual strain curves exhibit a late systolic peak (more than 60% of the RR interval), which is not physiological and likely the result of underestimation of the RR interval and errors in the DENSE analysis. Microvascular perfusion will influence our diffusion measurements in vivo, in particular mean diffusivity (47), although it does not appear to substantially affect principal eigenvector orientation significantly (25).

CONCLUSIONS

The currently accepted model of strain correction for diffusion data obtained with a STEAM-EPI sequence does not significantly alter measures relating to the primary eigenvector (HA and TA). However, it has a considerable effect on the orientation of the secondary eigenvector (E2A). In vivo E2A values without strain correction approximate more closely to the strain-free ex vivo values in a relaxed diastolic-like and

contracted systolic-like states, than after strain correction. A more complete model of dynamic myocardial microstructure is needed to enable accurate strain correction, taking into account cellular rearrangement and sheetlet shear.

REFERENCES

- Pettigrew JB. On the arrangement of the muscular fibres in the ventricles of the vertebrate heart, with physiological remarks. *Phil Trans R Soc Lond B* 1864;154:445–500.
- Streeter DD Jr, Spotnitz HM, Patel DP, Ross J Jr, Sonnenblick EH. Fiber orientation in the canine left ventricle during diastole and systole. *Circ Res* 1969;24:339–347.
- Smerup M, Nielsen E, Agger P, et al. The three-dimensional arrangement of the myocytes aggregated together within the mammalian ventricular myocardium. *Anat Rec (Hoboken)* 2009;292:1–11.
- Harrington KB, Rodriguez F, Cheng A, Langer F, Ashikaga H, Daughters GT, Criscione JC, Ingels NB, Miller DC. Direct measurement of transmural laminar architecture in the anterolateral wall of the ovine left ventricle: new implications for wall thickening mechanics. *Am J Physiol Heart Circ Physiol* 2005;288:H1324–H1330.
- Sands GB, Gerneke DA, Hooks DA, Green CR, Smail BH, Legrice IJ. Automated imaging of extended tissue volumes using confocal microscopy. *Microsc Res Tech* 2005;67:227–239.
- Gilbert SH, Benoist D, Benson AP, White E, Tanner SF, Holden A V, Dobrzynski H, Bernus O, Radjenovic A. Visualization and quantification of whole rat heart laminar structure using high-spatial resolution contrast-enhanced MRI. *Am J Physiol Heart Circ Physiol* 2012;302:H287–H298.
- LeGrice IJ, Smail BH, Chai LZ, Edgar SG, Gavin JB, Hunter PJ. Laminar structure of the heart: ventricular myocyte arrangement and connective tissue architecture in the dog. *Am J Physiol Heart Circ Physiol* 1995;269:H571–H582.
- LeGrice IJ, Takayama Y, Covell JW. Transverse shear along myocardial cleavage planes provides a mechanism for normal systolic wall thickening. *Circ Res* 1995;77:182–193.
- Takayama Y, Costa KD, Covell JW. Contribution of laminar myofiber architecture to load-dependent changes in mechanics of LV myocardium. *Am J Physiol Heart Circ Physiol* 2002;282:H1510–H1520.
- Costa KD, Takayama Y, McCulloch AD, Covell JW. Laminar fiber architecture and three-dimensional systolic mechanics in canine ventricular myocardium. *Am J Physiol* 1999;276:H595–H607.
- Spotnitz HM, Spotnitz WD, Cottrell TS, Spiro D, Sonnenblick EH. Cellular basis for volume related wall thickness changes in the rat left ventricle. *J Mol Cell Cardiol* 1974;6:317–331.
- Axel L, Wedeen VJ, Ennis DB. Probing dynamic myocardial microstructure with cardiac magnetic resonance diffusion tensor imaging. *J Cardiovasc Magn Reson* 2014;16:89.
- Sonnenblick EH, Ross J, Covell JW, Spotnitz HM, Spiro D. The ultrastructure of the heart in systole and diastole. Changes in sarcomere length. *Circ Res* 1967;21:423–431.
- Hales PW, Schneider JE, Burton RAB, Wright BJ, Bollensdorff C, Kohl P. Histo-anatomical structure of the living isolated rat heart in two contraction states assessed by diffusion tensor MRI. *Prog Biophys Mol Biol* 2012;110:319–330.
- Holmes AA, Scollan DF, Winslow RL. Direct histological validation of diffusion tensor MRI in formaldehyde-fixed myocardium. *Magn Reson Med* 2000;44:157–161.
- Scollan DF, Holmes A, Winslow R, Forder J. Histological validation of myocardial microstructure obtained from diffusion tensor magnetic resonance imaging. *Am J Physiol* 1998;275:H2308–H2318.
- Scollan DF, Holmes A, Zhang J, Winslow RL. Reconstruction of cardiac ventricular geometry and fiber orientation using magnetic resonance imaging. *Ann Biomed Eng* 2000;28:934–944.
- Kung GL, Nguyen TC, Itoh A, Skare S, Ingels Jr NB, Miller DC, Ennis DB. The presence of two local myocardial sheet populations confirmed by diffusion tensor MRI and histological validation. *J Magn Reson Imaging* 2011;34:1080–1091.
- Helm PA, Tseng H-J, Younes L, McVeigh ER, Winslow RL. Ex vivo 3D diffusion tensor imaging and quantification of cardiac laminar structure. *Magn Reson Med* 2005;54:850–859.
- Helm P, Beg MF, Miller MI, Winslow RL. Measuring and mapping cardiac fiber and laminar architecture using diffusion tensor MR imaging. *Ann N Y Acad Sci* 2005;1047:296–307.

21. Teh I, Burton RAB, McClymont D, Capel RA, Aston D, Kohl P, Schneider JE. Mapping cardiac microstructure of rabbit heart in different mechanical states by high resolution diffusion tensor imaging. *Prog Biophys Mol Biol* 2016;121:85–96.
22. Nielles-Vallespin S, Mekkaoui C, Gatehouse P, et al. In vivo diffusion tensor MRI of the human heart: reproducibility of breath-hold and navigator-based approaches. *Magn Reson Med* 2013;70:454–465.
23. Nguyen C, Fan Z, Sharif B, He Y, Dharmakumar R, Berman DS, Li D. In vivo three-dimensional high resolution cardiac diffusion-weighted MRI: a motion compensated diffusion-prepared balanced steady-state free precession approach. *Magn Reson Med* 2014;72:1257–1267.
24. Stoeck CT, von Deuster C, Genet M, Atkinson D, Kozerke S. Second-order motion-compensated spin echo diffusion tensor imaging of the human heart. *Magn Reson Med* 2016;75:1669–1676.
25. Scott AD, Ferreira PFADC, Nielles-Vallespin S, Gatehouse P, McGill L-A, Kilner P, Pennell DJ, Firmin DNDN. Optimal diffusion weighting for in vivo cardiac diffusion tensor imaging. *Magn Reson Med* 2015;74:420–430.
26. Aliotta E, Wu HH, Ennis DB. Convex optimized diffusion encoding (CODE) gradient waveforms for minimum echo time and bulk motion-compensated diffusion-weighted MRI. *Magn Reson Med* 2017;77:717–729.
27. Dou J, Reese TG, Tseng W-YI, Wedeen VJ. Cardiac diffusion MRI without motion effects. *Magn Reson Med* 2002;48:105–114.
28. Ferreira PF, Kilner PJ, McGill L-A, et al. In vivo cardiovascular magnetic resonance diffusion tensor imaging shows evidence of abnormal myocardial laminar orientations and mobility in hypertrophic cardiomyopathy. *J Cardiovasc Magn Reson* 2014;16:87.
29. Stoeck CT, Kalinowska A, von Deuster C, et al. Dual-phase cardiac diffusion tensor imaging with strain correction. *PLoS One* 2014;9:e107159.
30. Nielles-Vallespin S, Khalique Z, Ferreira PF, et al. Assessment of myocardial microstructural dynamics by in vivo diffusion tensor cardiac magnetic resonance. *J Am Coll Cardiol* 2017;69:661–676.
31. Edelman RR, Gaa J, Wedeen VJ, Loh E, Hare JM, Prasad P, Li W. In vivo measurement of water diffusion in the human heart. *Magn Reson Med* 1994;32:423–428.
32. von Deuster C, Stoeck CT, Genet M, Atkinson D, Kozerke S. Spin echo versus stimulated echo diffusion tensor imaging of the in vivo human heart. *Magn Reson Med* 2016;76:862–872.
33. Scott AD, Nielles-Vallespin S, Ferreira P, Khalique Z, McGill L-A, Kilner PJ, Pennell DJ, Firmin D. In-vivo cardiac DTI: an initial comparison of M012 compensated spin-echo and STEAM. *J Cardiovasc Magn Reson* 2016;18:W19.
34. Nguyen C, Speier P, Bi Xiaoming, Li D. Comparison between spin echo and stimulated echo diffusion encoding for diffusion-weighted cardiac magnetic resonance (DW-CMR) at 3T. In Proceedings of the 24th Annual Meeting of the ISMRM, Singapore, 2016.
35. Reese TG, Weisskoff RM, Smith RN, Rosen BR, Dinsmore RE, Wedeen VJ. Imaging myocardial fiber architecture in vivo with magnetic resonance. *Magn Reson Med* 1995;34:786–791.
36. Reese, Wedeen, Weisskoff. Measuring diffusion in the presence of material strain. *J Magn Reson B* 1996;112:253–258.
37. Tseng WY, Reese TG, Weisskoff RM, Wedeen VJ. Cardiac diffusion tensor MRI in vivo without strain correction. *Magn Reson Med* 1999;42:393–403.
38. McGill L-A, Ismail TF, Nielles-Vallespin S, et al. Reproducibility of in-vivo diffusion tensor cardiovascular magnetic resonance in hypertrophic cardiomyopathy. *J Cardiovasc Magn Reson* 2012;14:86.
39. Tunncliffe EM, Scott AD, Ferreira P, Ariga R, McGill L-A, Nielles-Vallespin S, Neubauer S, Pennell DJ, Robson MD, Firmin DN. Inter-centre reproducibility of cardiac apparent diffusion coefficient and fractional anisotropy in healthy volunteers. *J Cardiovasc Magn Reson* 2014;16:31.
40. Ferreira PF, Nielles-Vallespin S, de Silva R, et al. Study on the impact of strain correction on the secondary eigenvector of diffusion with in vivo and ex vivo porcine hearts. In Proceedings of the 20th Annual Meeting of the Society for Cardiovascular Magnetic Resonance, Washington DC, 2017.
41. Zhong X, Spottiswoode BS, Meyer CH, Kramer CM, Epstein FH. Imaging three-dimensional myocardial mechanics using navigator-gated volumetric spiral cine DENSE MRI. *Magn Reson Med* 2010;64:1089–1097.
42. Auger DA, Zhong X, Epstein FH, Meintjes EM, Spottiswoode BS. Semi-automated left ventricular segmentation based on a guide point model approach for 3D cine DENSE cardiovascular magnetic resonance. *J Cardiovasc Magn Reson* 2014;16:8.
43. Spottiswoode BS, Zhong X, Hess AT, Kramer CM, Meintjes EM, Mayosi BM, Epstein FH. Tracking myocardial motion from cine DENSE images using spatiotemporal phase unwrapping and temporal fitting. *IEEE Trans Med Imaging* 2007;26:15–30.
44. Gilliam AD, Suever JD, and contributors. 2016. DENSEanalysis. Retrieved from <https://github.com/denseanalysis/denseanalysis>.
45. Rüssel IK, Tecelão SR, Kuijer JPA, Heethaar RM, Marcus JT. Comparison of 2D and 3D calculation of left ventricular torsion as circumferential-longitudinal shear angle using cardiovascular magnetic resonance tagging. *J Cardiovasc Magn Reson* 2009;11:8.
46. Sosnovik DE, Wang R, Dai G, Wang T, Aikawa E, Novikov M, Rosenzweig A, Gilbert RJ, Wedeen VJ. Diffusion spectrum MRI tractography reveals the presence of a complex network of residual myofibers in infarcted myocardium. *Circ Cardiovasc Imaging* 2009;2:206–212.
47. Delattre BMA, Viallon M, Wei H, Zhu YM, Feiweier T, Pai VM, Wen H, Croisille P. In vivo cardiac diffusion-weighted magnetic resonance imaging: quantification of normal perfusion and diffusion coefficients with intravoxel incoherent motion imaging. *Invest Radiol* 2012;47:662–670.

SUPPORTING INFORMATION

Additional Supporting Information may be found in the online version of this article.

Fig. S1. Simulated diffusion tensors and the respective HA, E2A, and TA maps and histograms with and without strain correction for a diastolic and systolic tensor conformation.

Table S1. Numerical Simulations: Effects of Strain Correction on DTI Parameters

HA range, mean angle range from endocardium to epicardium; TA and E2A, median of the absolute values of all myocardial voxels.

Table S2. Summary of the Effects of Each Strain Direction to HA Range and E2A

Note: The TA is not affected considerably by any strain direction. ↗, increase; ↘, decrease; —, no considerable effect.